

## Article

# Mineralogical Characteristics and Genetic Types of Pyrite with Different Occurrence: Constraints from Spectroscopy, Geochemistry and $\delta^{34}\text{S}$ Stable Isotopes

Shiyu Ma <sup>1</sup>, Miao Shi <sup>1,2,3,4,\*</sup>, Cun Zhang <sup>5</sup> and Qinyuan Cao <sup>1</sup><sup>1</sup> School of Geology and Material Science, Hebei GEO University, Shijiazhuang 050031, China; masy0107@163.com (S.M.); maxcaoqinyuan@163.com (Q.C.)<sup>2</sup> Hebei Key Laboratory of Green Development of Rock Mineral Materials, Hebei GEO University, Shijiazhuang 050031, China<sup>3</sup> Engineering Research Center for Silicate Solid Waste Resource Utilization of Hebei Province, Hebei GEO University, Shijiazhuang 050031, China<sup>4</sup> State Key Laboratory of Geological Processes and Mineral Resources, China University of Geosciences, Wuhan 430074, China<sup>5</sup> School of Materials Science and Engineering, Qilu University of Technology (Shandong Academy of Sciences), Jinan 250353, China; gemzhangc@qlu.edu.cn

\* Correspondence: miaober727@126.com

**Abstract:** Pyrite is widely distributed in the Earth's crust and oceanic systems, and it generally occurs as pentagonal dodecahedra, cubic, octahedral, idiomorphic crystals, or dense, massive, granular, and nodular aggregates. In this study, representative pyrite samples from Hunan, Fujian, Jiangxi, Anhui in China and from Peru were collected. By utilizing a range of analytical techniques, including petrography, X-ray diffraction, infrared spectrum, Raman spectrum, major and trace element analysis, as well as sulfur stable isotope analysis, we comprehensively depict the mineralogical and spectroscopic characteristics of pyrite, and the evolution processes of the physical and chemical conditions of mineralization can be qualitatively constrained. The spectroscopic results indicate all samples show a relatively narrow absorption band with weak to moderate intensity in the vicinity of  $343\text{ cm}^{-1}$ , which represents the bending vibration of the  $\text{Fe}-[\text{S}_2]^{2-}$  molecular bond. The Co content of pyrite exhibits the characteristics of a positive correlation with temperature and a negative correlation with oxygen fugacity, respectively. The  $\delta^{34}\text{S}$  isotopic compositions of colloidal pyrite are in the range of 0.03 to 0.67, which are close to meteoric sulfur and mantle sulfur compositions, while the  $\delta^{34}\text{S}$  values of nodular pyrite fall within the range of granite, indicating the characteristics of mixtures of sulfur sources are mainly related to magmatic activity. Our results provide insight into the formation mechanisms of pyrite in different environments, its mineralization, and the ore genesis of deposits. Moreover, the integrated analytical methods for pyrite are provided, which can define theoretical guidance for the exploration and development of mineral resources.



**Citation:** Ma, S.; Shi, M.; Zhang, C.; Cao, Q. Mineralogical Characteristics and Genetic Types of Pyrite with Different Occurrence: Constraints from Spectroscopy, Geochemistry and  $\delta^{34}\text{S}$  Stable Isotopes. *Minerals* **2024**, *14*, 52. <https://doi.org/10.3390/min14010052>

Academic Editor: Jiří Sejkora

Received: 10 November 2023

Revised: 5 December 2023

Accepted: 21 December 2023

Published: 30 December 2023



**Copyright:** © 2023 by the authors. Licensee MDPI, Basel, Switzerland. This article is an open access article distributed under the terms and conditions of the Creative Commons Attribution (CC BY) license (<https://creativecommons.org/licenses/by/4.0/>).

## 1. Introduction

Pyrite ( $\text{FeS}_2$ ) belongs to the equiaxial crystal system, with an NaCl-type crystal structure, and is the most common sulfide in the Earth's crust [1]. The different morphology and grain size characteristics of pyrite could reflect its different growth environments and processes. Autocrystalline pyrite is generally produced in shale cracks or matrix, and the idiomorphic pyrite in the matrix is either dispersed or aggregated into lenticular bands, but the amount of development is relatively small [2].

A previous investigation has shown pyrite generated in hydrothermal deposits was associated with other sulfide, oxide, quartz, and other minerals, and sometimes huge accumulations of pyrite deposits could be formed [3]. The crystal morphology of hydrothermal

pyrite showed the crystallization habits have changed continuously with the evolution of mineralization. Generally, when the sulfur fugacity in the hydrothermal fluid is high, pyrite is prone to form “e” or “o” crystal shape, accompanied by complex polymorphic crystals. However, under high oxygen fugacity and low sulfur fugacity conditions, this is conducive to the growth of an “a” single crystal [4]. In metamorphic rocks, pyrite is often formed as a newborn product of metamorphism, while in sedimentary rocks, coal strata and sedimentary deposits, pyrite is often produced in massive, nodules or lenticular form, and its formation is inextricably linked to the organic matter. Pyrite nodules and agglomerates were dominant during the sedimentary period, and a total of three types of frambooids pyrite, autotombs and pyrite-accounted filling organisms were observed microscopically [1].

Meanwhile, the crystal shape and grain pattern of pyrite also play a great role in the study of the pyrite formation environment. The appearance of striated and nodular pyrite indicates the transformation of physical and chemical conditions of the sedimentary environment into an acidic sulfide-reduced environment, which is conducive to the preservation and enrichment of organic matter [5]. While, the formation of cubic crystals implies pyrite formed under the conditions of low supersaturation, low sulfur fugacity, and insufficient supply of material is favored to cubic growth, and the span of pyrite formation temperatures for cubic forms is relatively large [6].

Ornamental pyrite crystals with economic value have been reported in many regions of China, such as Hunan, Hubei, Zhejiang, Anhui, and Guangdong Provinces, as well as Spain, the United States, Mexico, Peru, and so on. The representative pyrite samples studied in this paper were collected from Anhui, Fujian, Jiangxi, Hunan, and Peru, including different sedimentary and hydrothermal genesis types. Most of the previous studies have focused on specific origin or type of genesis of pyrite, and the data made by the previous researchers were still incomplete, especially for the analysis of pyrite specimens with multiple origins and genesis. Therefore, this investigation carried out spectroscopy, major and trace element analysis etc., on specimens of different genesis types, and then synthesized the characteristics of its deposits, aiming to provide implications for the research of pyrite for the future. The study of trace elements in pyrite is of great significance to the understanding of the genesis of metallic ore deposits such as gold deposits, and guiding the search for exploration. Moreover, it can also be used to predict the enrichment pattern of shale gas and provide theoretical guidance for the exploration and development of mineral resources [7–9].

## 2. Materials and Methods

### 2.1. Sample Description

Five typical samples were collected from Anhui, Fujian, Jiangxi, Hunan Provinces, China and Peru, respectively (Figure 1). Sample HTK-3 (Figure 1a) from Ruijin of Jiangxi Province has no obvious crystal shape, and its pyrite product shows the characteristics of multi-stage output. The ore types are mainly divided into pyrite-quartz vein type and pyrite-silicified rubble breccia type, respectively. The whole sample presents a copper-yellow color with the size of about  $3 \times 5$  cm, spherical, nodular, and dense internal crystal structures, and the concentric ring structure can be observed on the longitudinal section. Sample HTK-4 (Figure 1b) was collected from Shangbao in Hunan Province, which was situated in the center of the South China fold system. This specimen exhibits a prominent copper-yellow hue and measures a substantial size of approximately  $6.7 \times 4$  cm. It is intricately linked with quartz, displaying a fully intact cubic form. Notably, the cubic grain size demonstrates a considerable range of variation. Additionally, the surface of the sample bears visible longitudinal striations, adding to its distinctive characteristics. The surface is relatively clean and smooth, and the development of cubic {100} single crystals can be found. Sample HTK-2 (Figure 1c) from Fujian shows a brown color with a size of about  $7.4 \times 6$  cm, and the pyrite occurs in association with quartz and calcite. It has small particle size with a tiny deviation range. Overall, pyrite is cubic, granular, and scattered in the crystal clusters. Sample HTK-1 (Figure 1d) originates from Anhui, which is a prototypical

skarn-type copper-gold deposit. This region generates not only exemplary skarn deposits but also an array of porphyry deposits. Remarkably, in certain locations, both skarn and porphyry mineralizations converge, leading to the coexistence of these distinct geological features. Furthermore, the area is distinguished by the presence of numerous layered skarn orebodies and, notably, layered massive sulfide orebodies, highlighting the rich diversity and complexity of the mineral deposits in this locale. The sample shows typical characteristics of a size of  $2.1 \times 1$  cm, copper-yellow color, and symbiosis with calcite. The crystals are pentagonal dodecahedral, layered structure, with a certain gradient of flat and straight growth striations on the surface. The grain size is medium, and the range of variation is narrow. Sample HTK-5 (Figure 1e) is symbiotic with sphalerite from a high-sulfidation epithermal deposit in Peru, shows a copper-yellow color, and the pyrite is octahedral. The sphalerite can be observed in a red fluorescence crystal shape, the grain size is medium, and the range of variation is relatively large.

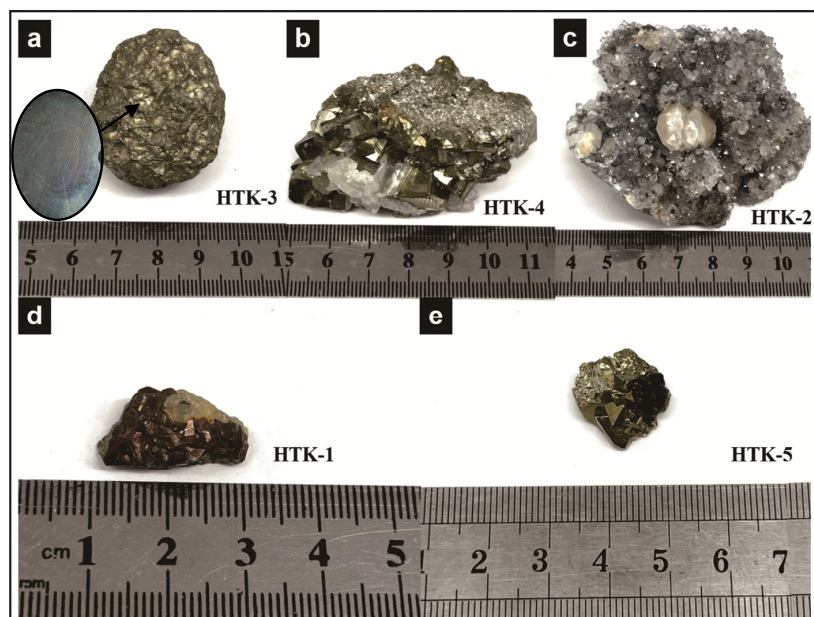


**Figure 1.** Macroscopic characteristics of pyrite samples: (a) HTK-3 occurs as concretions, and a concentric ring structure can be found on the longitudinal section, possibly having undergone synsedimentation. (b) HTK-4 occurs as a cube particle, and the pyrite occurs in association with quartz. (c) Sample HTK-2 is cubic and granular, with pyrite grains scattered in the crystal clusters. (d) Sample HTK-1 shows a pyritohedron shape, coexisting with calcite. (e) Sample HTK-5 is octahedral, in symbiosis with sphalerite which can be observed in red fluorescence.

## 2.2. Methods

A German Leica DW27009 polarizing microscope from the Jewelry Center Laboratory of Hebei GEO University was used to observe the internal structure and crystallization state of the minerals, then we circled the specific locations required for subsequent experiments; all the samples have been pretreated.

The reflectance method was used to detect the samples through a r1110 Nicolet Fourier infrared spectrometer instrument (Thermo Fisher Scientific, Waltham, MA, USA) in the Jewelry Center of Hebei GEO University. The wavelength range was set to  $400\text{--}4000\text{ cm}^{-1}$  with the scanning times and rates being 32 and  $4\text{ cm}^{-1}$ , respectively. The laboratory temperature was  $25^\circ\text{C}$ , and the humidity was 25% RH.

Raman spectroscopy of pyrite samples was performed at the Jewelry Center in Hebei GEO University, using a RENISHAW-Invia micro confocal laser Raman spectrometer from Renishaw, London, UK. The wavelength used was 532 nm. We used a scanning time of 20 s of spectrum in an extending mode spanning  $200\text{--}3000\text{ cm}^{-1}$ . The laboratory temperature was  $25^\circ\text{C}$ , and the humidity was 25% RH.

The X-ray fluorescence spectrometer model X-3680 from Tsushima Company, Nagasaki of Japan, was used in the Jewelry Center of Hebei GEO University, using an EDX-7000 energy dispersive X-ray fluorescence spectrometer. Each sample was tested using the Al-U channel and Na-Sc channel, respectively. And, the testing conditions were a tube voltage of 50 kV and 15 kV, respectively, while the tube current was set to 767  $\mu$ A and 1000  $\mu$ A, respectively. The time was 30 mm.

The X-ray powder crystal diffraction instrument was adopted from the Smart Lab Rigaku of Nihon, Hebei GEO University, China, with the following specific test conditions: copper target (Cu) test, emission and scattering slit of  $1^\circ$ , receiving slit of 0.3 mm, operating voltage of 48 kV, current of 1000 mA, scanning speed of  $6^\circ$  (20) min, and scanning range of  $2.6^\circ$ ~ $70^\circ$ .

The measurement of S isotope composition of the five samples was carried out at Wuhan Spectrum Analytical Technology Co., Ltd. (Wuhan, China). The instrument used is a multi-collector mass spectrometer model Neptune Plus MC-ICP-MS (Thermo Fisher Scientific, Waltham, MA, USA) and a coherent 193 nm excimer laser deposition system (Geo Las HD) to determine the material sources of the mineral, with a beam spot of 44  $\mu$ m, an energy intensity of 6 MJ/cm<sup>2</sup>, a frequency of 2 Hz, and a carrier gas of 500 mL/min.

### 3. Results and Discussion

#### 3.1. Pyrite Occurrence

The structural features of the samples could be clearly observed as in Figure 2.

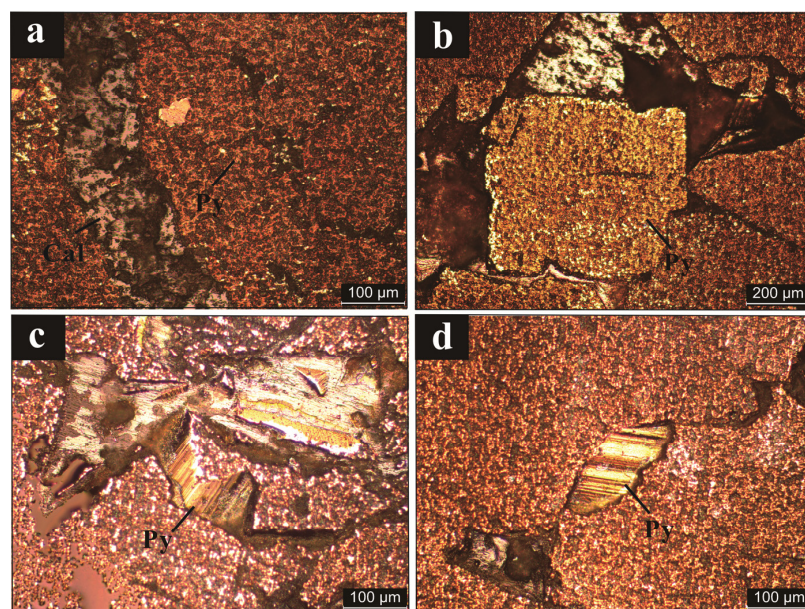


**Figure 2.** Representative photomicrographs showing different forms of pyrite. (a) Nodular pyrite in sample HTK-3. (b) Cubic pyrite in sample HTK-4. (c) Euhedral grains in sample HTK-2, and crystal face striations are visible. (d) Heteromorphic pyrite in sample HTK-1, and crystal face striations are also visible.

The whole sample HTK-3 (Figure 2a) presents an interwoven structure, while the crystals cannot be observed clearly. Generally, the structure is relatively dense, and the concentric ring structure can be observed on the longitudinal section, indicating its formation process is characterized by multiple phases [10]. The white minerals are distributed in stripes in the fissures, presumed to be calcite. The colloidal pyrite in Ruijin of Jiangxi Province was closely related to the activity of anaerobic microorganisms and the induced changes of sedimentary environment and pH [11]. Thus, the appearance of laminar and nodular pyrite represented the physical and chemical conditions of the depositional environment have been changed into an acidic sulfide-reduced environment, which was conducive to the preservation and enrichment of organic matter, corresponding to previous

studies [12]. The surface of the pyrite crystals is relatively rough due to the abrasion and carving effects during the process of deposition, transportation, and diagenesis [13,14]. In sample HTK-4, a large amount of authigenic pyrite can be observed, the symbiotic minerals which are presumed to be the chlorite, can be found to be in different shades of blue mixed with pyrite under a single polarized light microscope (Figure 2b). The parallel crystal surface streaks were clearly evident. Combined with the hand specimen, it can be inferred the pyrite is mostly in the shape of a cube, which reflects the ore-forming fluids may be in the low sulfur fugacity, high oxygen fugacity, high temperature, or middle temperature environments. In sample HTK-1 (Figure 2d), pyrite is observed in two different colors of copper-yellow and brown-yellow, with light brown as its tarnish. Combined with the hand specimen, the sample is a pentagonal dodecahedral agglomerate, indicating the mineralized fluid may have been in a medium-temperature environment with a high sulfur concentration. The rest of the samples have obvious crystalline grains, higher crystallinity, and are exhibited in granular and massive structures. Besides, crystalline grains can be observed in both light and dark basal parts clearly, and the relatively brighter position is the area where the crystalline grains are more concentrated when observed under polarized light.

Meanwhile, through the observation of backscattering images (BSE), it was found the sample HTK-2 contained colloidal pyrite (Figure 3). Chen et al. (1989) studied the mineralogy of pyrite genesis in the Jiaodong gold deposits and concluded the pyrite precipitated in the low-temperature late stage of hydrothermal mineralization, suggested a higher probability of occurrence of pyrite in the form of cubes, and was mostly produced in the low-temperature and surface conditions [13]. Xie et al. (2021) initially investigated the microscopic structure of colloidal pyrite, and concluded there were hydrothermal and sedimentary colloidal pyrite in the Baochun deposits, with the former produced in the form of veins and the latter produced in the form of calcite grains [14]. The pyrite with fine particles in the sample HTK-2 is distributed in cubic shape on the crystal clusters, it can be discovered the crystal clusters are more complete, and the calcite particles are larger, so it is assumed the formation environment is more stable, and it is justified to be a low-temperature, surface environment [15,16].

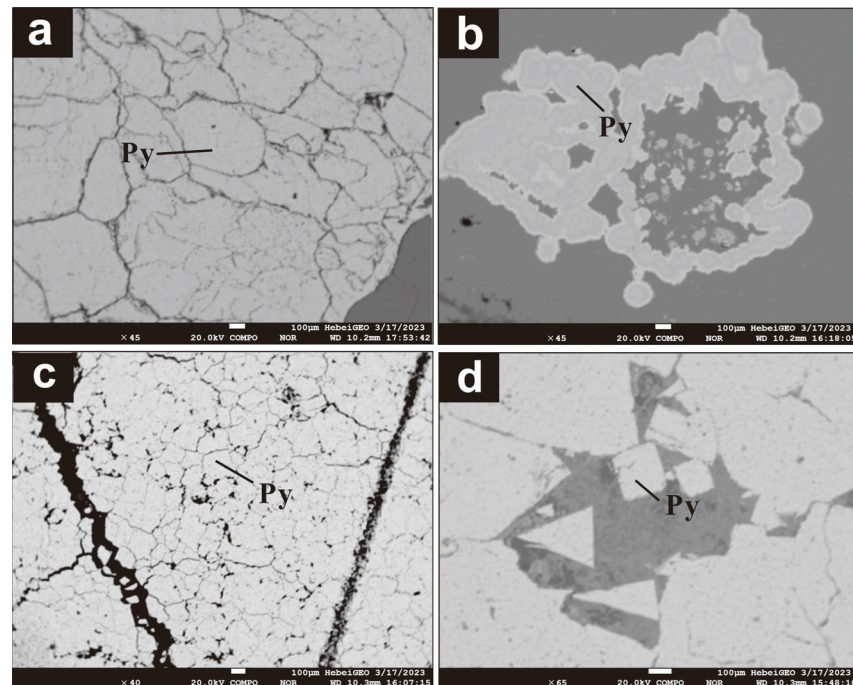


**Figure 3.** Representative photomicrographs of Backscatter Electron images (BSE), showing different growth habits of pyrite samples. (a) Euhedral grains in sample HTK-1. (b) Colloform pyrite in sample HTK-2. (c) Concretions in sample HTK-3. (d) Clearly cubic grains in sample HTK-4.

### 3.2. X-ray Diffraction Analysis

The five samples were analyzed by X-ray diffraction, and the diffraction peaks of pyrite, crystal, and other minerals can be detected. The distinction is the intensity of the diffraction peaks of the same minerals is distinguished in different samples, which indicates the relative contents of the minerals in the samples differ from each other (Figure 4).

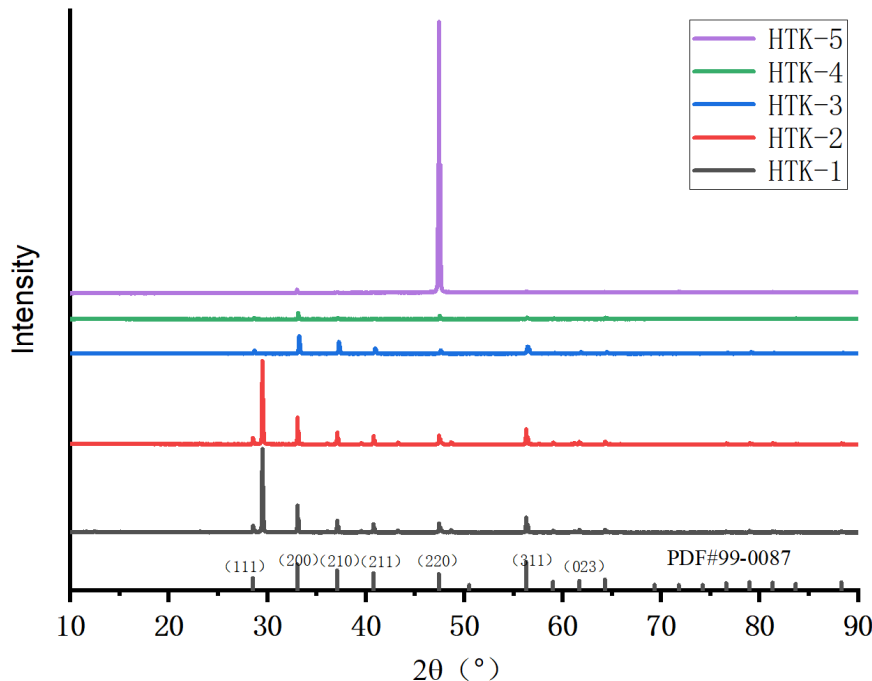


**Figure 4.** XRD diffraction pattern of samples. The diffraction peaks of  $28.62^\circ$ ,  $33.13^\circ$ , and  $40.86^\circ$  can be observed in the five samples, which are basically consistent with the standard pyrite card (PDF#71-2219). Moreover, the diffraction peaks of phlogopite with different degrees exist around  $47.44$  and  $56.36^\circ$ .

Compared with the spectrum peaks with the standard database of pyrite card (PDF#99-0087), the spectrums of samples are basically inconsistent with other coexisting minerals [17,18]. Peaks of different intensities of pyrite {200} crystal plane and {311} crystal plane are visible in all five samples [19]. Diffraction peaks of sphalerite (PDF#99-0097) were detected at  $29.49^\circ$  in addition to pyrite in sample HTK-3 and sample HTK-4. Besides, the structure of the belt in the sample HTK-3 is obvious, and the dark belt contains more marcasite. The relative intensity of the diffraction peaks in sample HTK-2 is weak, indicating characteristics of poor crystallinity. Almost no other peaks are visible except for the diffraction peaks in the standard card of pyrite, indicating its high purity and no other co-occurring minerals during the growth process [19]. The higher intensity of sample HTK-5 on crystal surface of {220}, the spectrum of the peak is sharper, revealing the pyrite sample crystallization degree is more intact. It shows a minor portion of the diffraction peaks displacement phenomenon, which is caused by other impurity ions into the lattice resulted from lattice defects and changes in the degree of crystallization caused by the mixing, respectively.

### 3.3. Infrared Spectrum Analysis

The infrared absorption peaks of pyrite are mainly caused by the stretching and bending vibration of Fe-S. The samples were tested for IR spectra separately, and the IR absorption spectra were shown in Figure 5 [19]. Compared with the absorption peak at  $407\text{ cm}^{-1}$  of the standard spectrum, the spectrum wave number of pyrite in the samples was shifted to the low-frequency region, where was the stretching and bending vibration of  $\text{Fe}^{2+}-[\text{S}_2]^{2-}$  in the fingerprint region. This shift may be caused by the contained impurities. Once the Fe or S is replaced by impurity elements in pyrite, it changes the intensity and

frequency of the resonance absorption, thus changing the characteristics of the infrared absorption spectrum. The intensity of the absorption peak at  $440\text{ cm}^{-1}$  which has shift to the low-frequency region is larger for sample HTK-3. Combined with trace element test results, it is indicated the substitution of Co and Ni for Fe is larger. And, the absorption peaks of sample HTK-3, sample HTK-1, and sample HTK-5 in this region are more intense, suggesting they contain more symbiotic minerals. While the spectrum of sample HTK-4 is generally smoother, indicating the sample contains less impurity minerals.

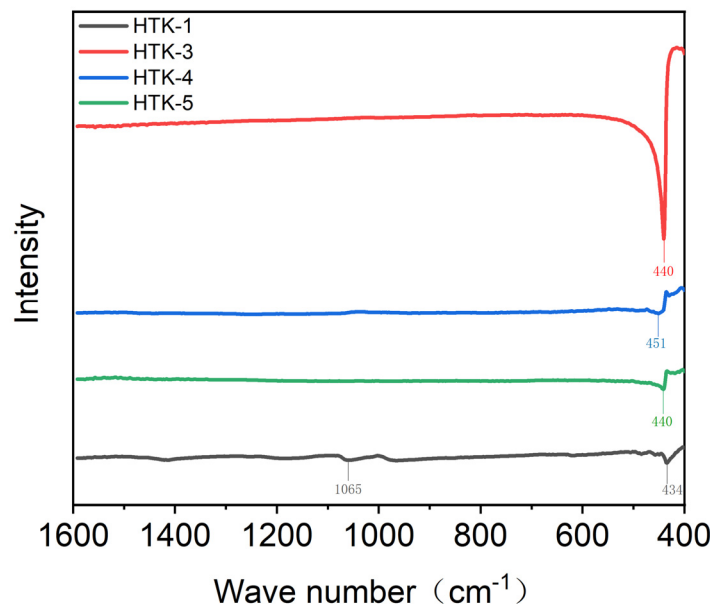


**Figure 5.** Infrared absorption spectra of each sample. The absorption peaks of different intensities were found at  $440\text{ cm}^{-1}$ , and the absorption intensity of HTK-3 was stronger. A weak absorption peak at  $1065\text{ cm}^{-1}$  can be found in sample HTK-1, and the absorption curves of HTK-4 and HTK-5 are relatively gentle.

### 3.4. Raman Spectrum Analysis

The results of Raman spectroscopy show three dominant characteristic peaks of pyrite with a strong peak at  $341\text{ cm}^{-1}$ , a strong peak at  $376\text{ cm}^{-1}$ , and a weak peak at  $430\text{ cm}^{-1}$ , which is attributed to the S-S stretching vibration peak [20]. By comparing the sample data with the standard spectrum, we can observe the lower half-height width (FWHM) of peaks of pyrite indicates a higher degree of crystallinity and order, and the lower formation temperature [20].

The results of Raman spectra are plotted in Figure 6. The standard Raman spectrum of pyrite mainly consists of the three following characteristic peaks. In the vicinity of  $343\text{ cm}^{-1}$ , all the samples show relatively narrow absorption bands of weak to moderate intensity, which represents the bending vibration of the  $\text{Fe}-[\text{S}_2]^{2-}$  molecular bond (Eg). In the vicinity of  $376\text{ cm}^{-1}$ , all the samples show narrow absorption bands of moderate to strong intensity, suggesting the stretching vibration of  $\text{Fe}[\text{S}_2]^{2-}$  molecular bonds (Ag) in pyrite. According to a previous study, the characteristic Raman shift of pyrite in the vicinity of  $379\text{ cm}^{-1}$  can effectively reveal the crystallinity of pyrite and its degree of ordering, and if the FWHM is smaller, it means the pyrite exhibits a higher degree of ordering and crystallinity [20]. However, near  $430\text{ cm}^{-1}$ , some samples show weaker intensity and narrower absorption band, indicating the stretching vibration of the S-S bond (Tg) inside the  $[\text{S}_2]^{2-}$  anion cluster in complex sulfides.

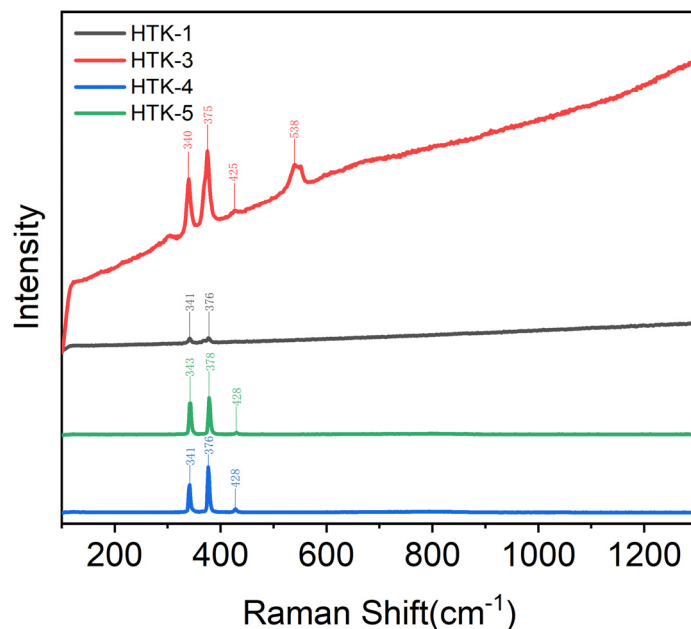


**Figure 6.** Raman spectra of each sample. Samples show different intensity absorption peaks around  $341\text{ cm}^{-1}$  and  $376\text{ cm}^{-1}$ , among which the HTK-3 sample also shows a strong absorption peak at  $538\text{ cm}^{-1}$ .

Therefore, combined with the probe analysis results, it can be inferred the shifts of Raman spectra peaks of different crystal morphology may be mainly related to the growth environment. The morphology of pyrite can reflect the change of physical and chemical properties of ore-forming fluid well, and the crystal morphology of pyrite in different ore-forming stages is obviously different. Generally, the sample HTK-1 which is pentadodecahedral polygonal shows the weakest absorption intensity and is missing the absorption peak near  $430\text{ cm}^{-1}$ , while the lower FWHM indicates poorer ordering and crystallinity and a higher formation temperature at this location. The Sample HTK-3 which is a nodular structure presents the strongest absorption intensity and broader FWHM, suggesting the degree of crystallinity and order is low. The intensity and FWHM of samples HTK-4 and HTK-5 are quite similar, so it can be inferred the formation temperatures and pressures of pyrite from Shangbao of Hunan Province and Peru may have similar characteristics. The sample HTK-5 presents almost no change in the position of the intensity peak at  $343\text{ cm}^{-1}$ , indicating the Fe-[S<sub>2</sub>]<sup>2-</sup> groups are more stable and less likely to be replaced by other anion groups.

All samples show characteristic peaks near  $341\text{ cm}^{-1}$ ,  $376\text{ cm}^{-1}$ , and  $430\text{ cm}^{-1}$  in the characteristic fingerprint area, which indicates the overall samples are pyrite mineral phases. Raman spectra of the pyrite in this area reflects the changes of the bond lengths and angles, and in turn, these changes in chemical bonds can also imply the temperature and pressure conditions of its formation [8]. In general, the lithostatic pressure is the main force on the mineralizing fluid. With the increase of depth, the lithostatic pressure of the overlying rock layer increases, the pressure of the crystallization of minerals in the mineralizing fluid increases, while the bond length of the crystal atoms is shortened accordingly, and the force constants increase. Thus, the Raman spectrum peaks of the minerals are shifted to higher frequency. The peaks of all samples present a shift to the left to a certain extent, while the left shift of the sample HTK-3 is more obvious. Combined with the test results of Co and Ni elements below, we could infer it was formed in a deeper depth and higher pressure environment. Finally, it could be concluded the sample HTK-3 was formed in a high-temperature sedimentary environment. The peak of pyrite spectrum at  $324\text{ cm}^{-1}$  can be observed in the Raman spectrum of sample HTK-3, which is consistent

with the results of the XRD test, suggesting the formation of colloidal pyrite is related to marcasite, and an acidic environment is more likely to occur here.

### 3.5. Major and Trace Elements Analysis

#### 3.5.1. Major Elements Analysis

According to the contents of Fe and S elements of pyrite, the morphology can be determined. The pyrite samples were analyzed by electron microprobe analysis (EMPA) for the main quantitative elements, with w(Fe) 45.78% and w(S) 53.12% in the sample HTK-1, w(Fe) 45.99% and w(S) 53.43% in the sample HTK-2, and w(Fe) 46.16% and w(S) 53.59% in the sample HTK-4, w(Fe) 45.81% and w(S) 53.97% in the sample HTK-5, respectively. The theoretical value of w(Fe) is 46.55%, and the content of w(S) is 53.45% [21]. When the ratio of S/Fe is less than 2, it is called a sulfur deficit, while the ratio of S/Fe is greater than 2, it is called an iron deficit. The two samples are attributed to an iron deficit of comparable degree, which is consistent with the hydrothermal gold deposit of pyrite in the hydrothermal type [21]. The sample HTK-3 contained w(Fe) 46.56%, w(S) 51.88% which was attributed to being Fe-rich and S-poor compared with the sulfur and iron contents in the metal ores formed by sedimentation and the theoretical values [w(Fe) = 46.16%, w(S) = 53.84%], indicating the depositional environment was one of oxygenated bottom water overlying oxygen-poor sediments, with bacterial sulfate reduction occurring below the sediment-water interface, and possibly formed in a higher temperature environment.

#### 3.5.2. Trace Elements Analysis

As one of the important gold-carrying minerals, pyrite is rich in a variety of trace elements, such as Au, Ag, Pb, Zn, Cu, Mo, Co, Ni, As, Sb, Se, Te, Bi, Tl, and Hg, which are closely related to the genesis of gold mineralization [22]. They are mainly presented in pyrite in the form of solid solutions, invisible inclusions at the nanometer scale, and visible inclusions at the micrometer scale endowed in the pyrite lattice or in pyrite.

Generally, the pyrite generated from magmatic hydrothermal gold deposits is enriched in high-, medium-, and low-temperature elements such as Ti, Cr, Mo, and Hg, and the pyrite from volcanic hydrothermal gold deposits is enriched in medium-temperature elements such as Mo and Sn [23]. The pyrite from metamorphic hydrothermal gold deposits is enriched in elements such as Ti and Cr, whereas pyrite from Carlin-type gold deposits is enriched in low-temperature elements such as Tl, Zn, and Hg [24]. Moreover, elements such as Se and Te are mainly enriched in volcanic and magmatic hydrothermal gold deposits, and elements such as Sb and Bi mainly occur in metamorphic hydrothermal gold deposits [25].

In our present study, microscopic observation shows sphalerite and galena inclusions are often observed in pyrite during the metallogenic period, while relatively small pyrite inclusions are also discovered in large-grained sphalerite, and Pb, Cu, and Zn in pyrite are mainly in the form of galena, sphalerite, and chalcopyrite.

The trace elements analytical results of pyrite are listed in Table 1, and the analysis results show pyrite from different origins shows distinct trace elements characteristics.

The results show the contents of trace elements in the sample HTK-3 were high except Co, Ni, Pb, and Cu, and the other elements were low. The contents of Co and Ni in pyrite are related to the high concentration of components in the forming medium and the physical and chemical conditions of their formation, respectively. It has been shown the Co content in pyrite showed a positive correlation with temperature [26], and a negative correlation with oxygen fugacity, so it could be inferred the sample HTK-3 was formed at higher temperature and lower oxygen fugacity. In addition, the sample HTK-3 with nodular and concentric ring structure can be discovered in the longitudinal profile, which suggests it has undergone the same deposition process. Combined with the characteristics of trace elements, it was inferred sample HTK-3 has undergone two stages of sedimentation and diagenesis. The presence of elements such as Au and Ag in pyrite may depend on the mineral inclusions, which is sometimes finely dispersed.

**Table 1.** Analytical data of major and trace elements in pyrite ( $\times 10^{-6}$ ). Three test points were selected for each sample.

Number	HTK-1-1	HTK-1-2	HTK-1-3	HTK-3-1	HTK-3-2	HTK-3-3	HTK-4-1	HTK-4-2	HTK-4-3
S	313,282	182,869	1436.13	1,916,226	282,969	140,255	38,785,600	39,412,100	4,149,543
Cr	1.25	1.21	115.67	2.71	2.23	8.28	3054.49	1319	1622
Fe	1,452,510	1,531,390	13,285	1,408,446	1,397,150	1,272,798	10,446,837	10,422,333	11,208,000
Co	0.27	1.55	22.42	114.09	3.83	92.27	2948	52,811	134,578
Ni	2.25	11.03	73.14	68.06	3.15	115.47	1902	84.49	71.91
Cu	0.10	0.14	2.39	67.91	6.03	20.38	255.9	191.20	81.71
Zn	1.13	1.23	34.99	6.23	4.61	7.85	194.4	33.50	53.06
As	1926	1992	38.27	7.51	6.22	10.88	5415	6680	23,496
Se	-0.14	-0.04	4.05	0.81	0.86	0.72	31.15	32.51	61.23
Ag	0.00	0.00	6.35	1.40	0.03	0.35	63.62	127.4	-1.78
Sb	20.24	21.77	10.91	0.55	0.11	0.69	108.8	285.15	249.4
Te	0.00	0.00	-0.30	-0.01	-0.01	-0.01	70.66	338.9	1892
Au	0.00	0.00	-0.24	0.00	0.00	0.00	6.00	6.39	-3.91
Hg	-	-	-	-	-	-	122.5	102.3	114.5
Tl	0.28	0.88	1.32	0.15	0.06	0.09	-3.42	7.96	3.50
Pb	0.01	0.04	69.37	52.36	15.64	51.72	1807	8037	478.8
Bi	0.00	0.00	10.28	0.01	0.00	0.03	27,174	46,509	830.9

Both the sample HTK-1 and HTK-4 are associated with quartz and produced in automorphic to semi-automorphic form. The contents of As, Se, and Tl are relatively high in both samples (Table 1). The sample HTK-1 presents a pentagonal dodecahedron with high content of low-temperature elements such as Tl and Zn, suggesting it exhibits Carlin hydrothermal pyrite characteristics. The sample HTK-4 with cubic shape shows a high degree of automorphism. It can be observed pyrite is large particle with a cube structure, and the content of Cr, Hg, and other low-temperature elements is relatively high. It is speculated it should be attributed to magmatic hydrothermal pyrite type.

Generally, the volcanic-hydrothermal pyrite is rich in Mo and Sn medium-temperature elements, and the magmatic-hydrothermal pyrite is rich in Ti, Cr, Mo, Hg, and other high- and low-temperature elements. While the metamorphic-hydrothermal pyrite is rich in high-temperature elements such as Ti and Cr [25]. Besides, As, Ni, Co, Sb, Se, Mo, and other elements are generally uniformly distributed in pyrite, directly into the crystal structure or mixed at nanometer level. Elements such as Bi, Pb, Ag, Au, Te, Cu, and other elements are mixed with pyrite at low density, but can enter the pyrite lattice at high concentration. Zn and Cd elements are in sphalerite microcrystals of pyrite, and their contents vary greatly [27]. The sample HTK-1 shows high As and Sb contents and low Co content. The lattice distortion caused by the addition of As greatly improves the efficiency of Au adsorption by pyrite and may determine the dissolution limit of Au in pyrite. Therefore, the Au in pyrite is usually positively correlated with the As content for most hydrothermal gold deposits [25]. The Co content is affected by the temperature and the oxygen fugacity of the fluids, which suggests it may be formed at lower temperature, higher oxygen fugacity environments. In the sample HTK-1, the trace element contents are generally higher than other samples, especially Co, As, and Bi elements, and the present study shows the Au and Sb contents of pyrite show significant positive correlation [28], which indicates the trace element contents in pyrite crystallized in high-temperature environment are usually higher and richer in variety. While the pyrite crystallized in low-temperature environment implies fewer varieties of trace elements and lower content.

#### 4. S Stable Isotope

Based on S stable isotope characteristics, four main sources of sulfur are proposed: (1) primitive sulfur, which comes from sulfur directly released by magma in the mantle or sulfur leaching from magma sulfide, with  $\delta^{34}\text{S}$  value close to 0‰, indicating sulfur in the metallogenetic fluids exists in single source; (2) seawater and oceanic evaporites, with a

$\delta^{34}\text{S}$  value of about 20‰; (3) mixture of sulfur, with a  $\delta^{34}\text{S}$  value of about 5‰~15‰, which is a mixed source of mantle sulfur and seawater sulfate; (4) organic (bacterial) reduced genesis sulfur, when the  $\delta^{34}\text{S}$  value is negative, at this time, pyrite under open depositional conditions and belongs to sedimentary type [29].

In this study,  $\delta^{34}\text{S}$  stable isotopes were carried out on different pyrite production forms, including framboids, colloid, and euhedral grains, and the data are shown in Table 2 and plotted in Figure 7. The sulfides in the samples were all pyrite, and no other sulfate minerals formed under high oxygen fugacity were found, so the sulfur in the hydrothermal fluids mainly existed in the form of  $\text{S}^{2-}$ ,  $\text{H}_2\text{S}$ , and crystallized under the low-oxygen reduction conditions, and the  $\delta^{34}\text{S}$  values of pyrite could approximately reflect the total sulfur in the ore-forming hydrothermal fluid [30,31].

The  $\delta^{34}\text{S}$  value of colloidal pyrite in the sample HTK-2 is 0.15‰ to 2.37‰ with an extremely constrained range of variations, and the  $\delta^{34}\text{S}$  values are very close to the meteoric sulfur range and the mantle sulfur range ( $0\text{‰} \pm 3\text{‰}$ ) [31], indicating its  $\delta^{34}\text{S}$  stable isotopic compositions are relatively stable and the sulfur sources are homogeneous. The  $\delta^{34}\text{S}$  value of frambooidal pyrite shows wide range of variation between 6.21‰ and 30.86‰, and the sample HTK-3 (concretion) has  $\delta^{34}\text{S}$  values of 2.35‰ to 4.58‰, which mainly falls within the granite range, suggesting its sulfur source is mainly derived from magmatic activity [32,33]. Among them, the  $\delta^{34}\text{S}$  values of the sample HTK-1 (euhedral grains) are among 16.32‰ to 18.73‰, and the  $\delta^{34}\text{S}$  stable isotope characteristics are very similar to those in modern seawater, probably suggesting the magma obtaining heavy sulfur from seawater sulfate during underwater spate. Notably, the well-crystallized sample HTK-3 shows the heaviest  $\delta^{34}\text{S}$  isotopic composition. The  $\delta^{34}\text{S}$  values of euhedral pyrite in sedimentary rock are relatively high, with  $\delta^{34}\text{S}$  values ranging from 29.84‰ to 30.01‰, which mainly falls in the range of sedimentary rocks (~50‰~35‰), the high  $\delta^{34}\text{S}$  value can be considered magma degassing ( $\text{H}_2\text{S}$  relative deficit  $^{34}\text{S}$ ,  $\text{H}_2\text{S}$  degassing can lead to enriching  $^{34}\text{S}$  in melt), or partly due to the sources of seawater jet hydrothermal.

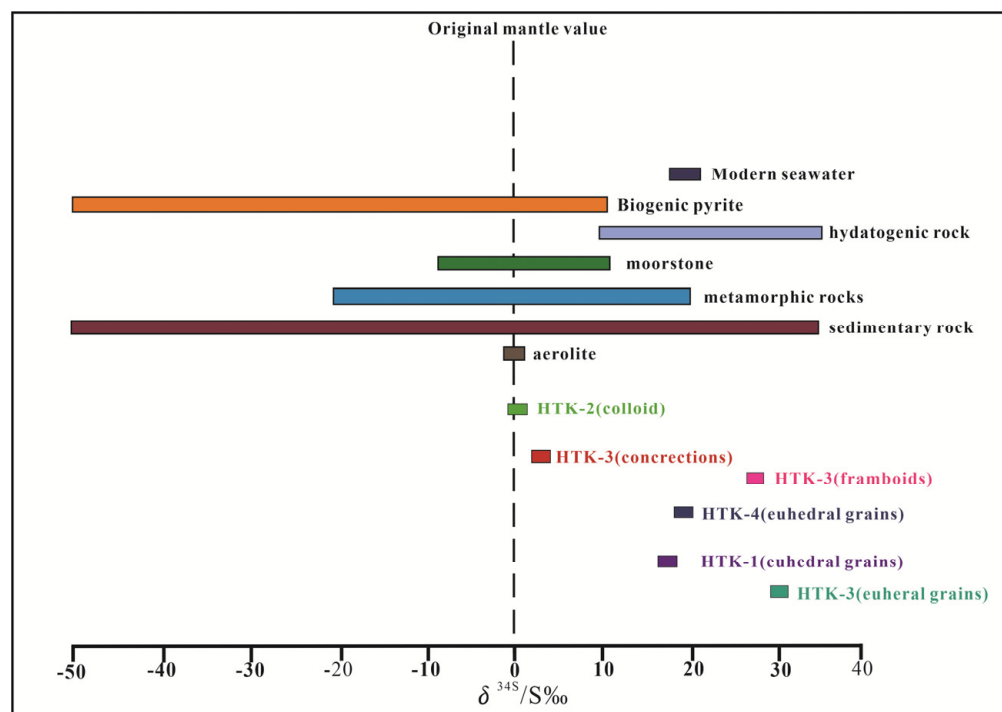


Figure 7. Diagram of  $\delta^{34}\text{S}$  stable isotope distribution in pyrite (modified after Li, 2016 [33]).

**Table 2.**  $\delta^{34}\text{S}$  values of pyrite with different occurrences in the present study.

Samples	Lithology	Mineral	Form	$\delta^{34}\text{S}\text{\%}$
HTK-3	sedimentary	Pyrite	euhedral grains	29.15~31.01
HTK-3	sedimentary	Pyrite	frambooids	5.32~7.01
HTK-3	sedimentary	Pyrite	frambooids	29.96~30.86
HTK-2	hydrothermal	Pyrite	colloid	0.15~2.37
HTK-3	sedimentary	Pyrite	concretions	2.35~4.58
HTK-4	hydrothermal	Pyrite	euhedral grains	18.34~20.92
HTK-1	hydrothermal	Pyrite	euhedral grains	16.32~18.73

## 5. Conclusions

- (1) The presence of nodular pyrite formed during sedimentary processes indicated the sedimentary environment has been transitioned into an acidic sulfide reduction environment, with deeper formation depths, higher environmental pressure, and higher temperatures. Spectral and trace element analyses show this type of pyrite exhibits significant substitution of Fe by Co and Ni elements, and the pyrite crystallized in this environment shows higher and more diverse trace element contents.
- (2) The cubic pyrite in hydrothermal genesis has high crystallinity and is predominated by coarse-grained euhedral pyrite in the early stages and fine-grained pyrite in the late stages of mineralization, respectively. The ore-forming fluids may be in low-sulfur and high-oxygen fugacity environment, with high As and Cr contents in pyrite. Pentagonal decahedral polycrystalline pyrite grown in layered structure with high-temperature morphological characteristics, so the ore-forming fluids could be in the high-sulfur-concentration medium-temperature environment with high As, Bi, Pb, and Cu contents. Meanwhile, the octahedral pyrite presents good crystallinity and fewer spectral peaks in its spectral characteristics, and magmatic activity controls the formation of the deposit.
- (3) The sulfur isotope compositions suggest the sulfur sources in sedimentary pyrite are mainly granite and sedimentary rocks, and the sulfate supply can be divided into two cases:  $\text{SO}_4^{2-}$  open system and  $\text{SO}_4^{2-}$  closed system, respectively. The sulfur sources of hydrothermal pyrite exhibit mixed sulfur characteristics, indicate a dominant mantle sulfur signature with mixture of seawater sulfate sources.

**Author Contributions:** Conceptualization, S.M. and M.S.; methodology, S.M. and M.S.; software, S.M.; validation, S.M., M.S. and C.Z.; formal analysis, S.M., M.S. and Q.C.; investigation, S.M. and Q.C.; resources, M.S.; data curation, S.M. and M.S.; writing—original draft preparation, S.M.; writing—review and editing, S.M., M.S. and C.Z.; supervision, Q.C.; project administration, S.M. and M.S.; funding acquisition, S.M. and Q.C. All authors have read and agreed to the published version of the manuscript.

**Funding:** This research was jointly funded by National Natural Science Foundation of China (Grant No.42002156), Natural Science Foundation of Hebei Province of China (Grant No.D2021403015), Science and Technology Project of Hebei Education Department (Grant No.QN2021027), The 19th student Science and Technology Fund research project of Hebei University of Geosciences (Grant No.KAY202311), and Hebei Province Key Laboratory of strategic key mineral resources open fund (Grant No.HGU-SCMR2316), and Hebei GEO University National Pre-research Project Funding(Grant No.KY2024YB01). The APC was funded by [National Natural Science Foundation of China], grant number [42002156], [Natural Science Foundation of Hebei Province of China], grant number [D2021403015], and [Science and Technology Project of Hebei Education Department], grant number [QN2021027].

**Data Availability Statement:** All data are contained within the work.

**Acknowledgments:** We are grateful to the Editor-in-Chief and the Academic Editors, as well as two anonymous reviewers for their constructive comments and suggestions that greatly improve this manuscript.

**Conflicts of Interest:** The authors declare they have no known competing financial interests or personal relationships that could have appeared to influence the work reported in this paper.

## References

1. Bragg, W.L. The Analysis of Crystals by the X-ray Spectrometer. *J. Proc. R. Soc. Lond.* **1914**, *613*, 468–489.
2. Cook, N.J. Mineralogy of the sulphide deposits at Sulitjelma, northern Norway. *J. Ore Geol. Rev.* **1996**, *5*, 303–338. [[CrossRef](#)]
3. Liu, J.; Li, S.; Li, Z.; Liu, Q.; Guo, W.; Zhou, X.; Ma, X. Development characteristics and geological significance of shale pyrite in Chang 7<sub>3</sub> submember of Ordos Basin. *Nat. Gas Geosci.* **2021**, *12*, 1830–1838.
4. Chu, F.Y.; Hu, D.Q.; Yu, H.L.; Yao, J. Significance of pyrite crystal morphology speciation in gold ore evaluation. *J. Jilin Univ. Earth Sci. Ed.* **2004**, *4*, 531–535.
5. Zhang, G.; Nie, H.; Tang, X.; Du, W.; Sun, C.; Chen, S. Types of pyrite in shales and their effects on shale gas enrichment-A case study of Wufeng Formation-Longmaxi Formation shales in the Sichuan Basin and its periphery. *Exp. Pet. Geol.* **2020**, *3*, 459–466.
6. Russo, R.E.; Mao, X.L.; Borisov, O.V.; Liu, H. Influence of wavelength on fractionation in laser ablation ICP-MS. *J. Anal. At. Spectrom.* **2000**, *9*, 1115–1120. [[CrossRef](#)]
7. Sack, P.J.; Large, R.R.; Gregory, D.D. Geochemistry of shale and sedimentary pyrite as a proxy for gold fertility in the Selwyn basin area, Yukon. *J. Miner. Depos.* **2018**, *7*, 997–1018. [[CrossRef](#)]
8. Shaheen, M.E.; Gagnon, J.E.; Fryer, B.J. Femtosecond (fs) lasers coupled with modern ICP-MS instruments provide new and improved potential for in situ elemental and isotopic analyses in the geosciences. *J. Chem. Geol.* **2012**, *330*, 260–273. [[CrossRef](#)]
9. Reich, M.; Kesler, S.E.; Utsunomiya, S.; Palenik, C.S.; Chrysoulis, S.L.; Ewing, R.C. Solubility of gold in arsenian pyrite. *J. Geochim. Cosmochim. Acta* **2005**, *11*, 2781–2796. [[CrossRef](#)]
10. Norris, A.; Danyushevsky, L. *Towards Estimating the Complete Uncertainty Budget of Quantified Results Measured by LA-ICP MS*; J. Goldschmidt: Boston, MA, USA, 2018.
11. Peterson, E.C.; Mavrogenes, J.A. Linking high-grade gold mineralization to earthquake-induced fault-valve processes in the Porgera gold deposit, Papua New Guinea. *J. Geol.* **2014**, *5*, 383–386. [[CrossRef](#)]
12. Chen, G.Y.; Shao, W.; Sun, D.S. *Genetic Mineralogy of Gold Deposits in Jiaodong Region with Emphasis on Gold Prospecting*; Chongqing Publishing House: Chongqing, China, 1989.
13. Xie, Q.; Sun, S.; Ma, Z.; Xu, L.; Wang, J.; Zhou, Y.; Chen, T.; Xu, X. Mineralogical and metallogenetic analysis of colloidal pyrite in the Baogungold (Cu) deposit, Tongling. *Acta Geol. Sin.* **2021**, *5*, 1481–1494.
14. Norman, M.; Robinson, P.; Clark, D. Major-and trace-element analysis of sulfide ores by laser-ablation ICP-MS, solution ICP MS, and XRF: New data on international reference materials. *J. Can. Mineral.* **2003**, *2*, 293–305. [[CrossRef](#)]
15. Müller, W.; Shelley, M.; Miller, P.; Broude, S. Initial performance metrics of a new custom-designed ArF excimer LA-ICPMS system coupled to a two-volume laser-ablation cell. *J. Anal. At. Spectrom.* **2009**, *2*, 209–214. [[CrossRef](#)]
16. Rickard, D.; Luther, G.W. Chemistry of iron sulfides. *J. Chem. Rev.* **2007**, *2*, 514–562. [[CrossRef](#)]
17. Mavrogonatos, C.; Voudouris, P.; Zaccarini, F. Multi-stage introduction of precious and critical metals in pyrite: A case study from the Kynos Hill and Pagoni Rachi porphyry/epithermal prospects, NE Greece. *J. Miner.* **2020**, *9*, 784. [[CrossRef](#)]
18. Yao, C.; Song, H.; Li, Q. Raman spectrum characterization of pyrite in the Jiaoja gold deposit in Jiaodong and its diagenetic significance. *Spectrosc. Spectr. Anal.* **2020**, *8*, 2479–2483.
19. Han, Q.M. Current status of pyrite physicochemical speciation characterization. *China Met. Bull.* **2019**, *6*, 188–190.
20. Huston, D.L.; Sie, S.H.; Suter, G.F.; Cooke, D.R.; Both, R.A. Trace elements in sulfide minerals from eastern Australian volcanically-hosted massive sulfide deposits; Part I, Proton microprobe analyses of pyrite, chalcopyrite, and sphalerite, and Part II, Selenium levels in pyrite; comparison with delta <sup>34</sup>S values and implications for the source of sulfur in volcanogenic hydrothermal systems. *Econ. Geol.* **1995**, *5*, 1167–1196.
21. Belousov, I.; Large, R.; Meffre, S.; Danyushevsky, L.; Steadman, J.; Beardmore, T. Pyrite compositions from VHMS and orogenic Au deposits in the Yilgarn Craton, Western Australia: Implications for gold and copper exploration. *J. Ore Geol. Rev.* **2016**, *79*, 474–499. [[CrossRef](#)]
22. Zhang, H.; Zhao, Q.; Zhao, G.; Hong, J.; Liu, J.; Zhai, D. Technical method for in situ microzonation analysis of pyrite trace elements by LA-ICP-MS and its application in the study of gold deposits. *Geol. Ore Depos.* **2023**, *6*, 1–18.
23. Yan, Y.; Li, S.; Jia, B.; Zhang, N.; Yan, L. Characteristics of metallogenetic speciation of pyrite composition during the metallogenetic period of gold deposits of different genesis types. *GOLD* **2012**, *3*, 11–16.
24. Román, N.; Reich, M.; Leisen, M.; Morata, D.; Barra, F.; Deditius, A.P. Geochemical and micro-textural fingerprints of boiling in pyrite. *Geochim. Cosmochim. Acta* **2019**, *246*, 60–85. [[CrossRef](#)]
25. Gregory, D.D.; Large, R.R.; Halpin, J.A.; Baturina, E.L.; Lyons, T.W.; Wu, S.; Danyushevsky, L.; Sack, P.J.; Chappaz, A.; Maslennikov, V.V.; et al. Trace element content of sedimentary pyrite in black shales. *J. Econ. Geol.* **2015**, *6*, 1389–1410. [[CrossRef](#)]
26. Li, W.; Cook, N.J.; Xie, G.Q.; Mao, J.W.; Ciobanu, C.L.; Li, J.W.; Zhang, Z.Y. Textures and trace element signatures of pyrite and arsenopyrite from the Gutaishan Au-Sb deposit, South China. *Miner. Depos.* **2019**, *4*, 591–610. [[CrossRef](#)]
27. Liu, Y.; Xie, H.; Xu, L.; Ni, Z.; Lu, F.; Tan, H. Sulfur isotope geochemical characteristics of Ziziping lead-zinc deposit in Jiulong County, Sichuan Province. *Geol. Bull. China* **2020**, *12*, 8.

28. Large, R.R.; Halpin, J.A.; Danyushevsky, L.V.; Maslennikov, V.V.; Bull, S.W.; Long, J.A.; Gregory, D.D.; Lounejeva, E.; Lyons, T.W.; Sack, P.J.; et al. Trace element content of sedimentary pyrite as a new proxy for deep-time ocean–atmosphere evolution. *J. Earth Planet. Sci. Lett.* **2014**, *389*, 209–220. [[CrossRef](#)]
29. Ohmoto, H. Systematics of sulfur and carbon isotopes in hydrothermal ore deposits. *Econ. Geol.* **1972**, *5*, 551–578. [[CrossRef](#)]
30. Keith, M.; Haase, K.M.; Klemd, R.; Krumm, S.; Strauss, H. Systematic variations of trace element and sulfur isotope compositions in pyrite with stratigraphic depth in the Skouriotissa volcanic-hosted massive sulfide deposit. Troodos ophiolite, Cyprus. *J. Chem. Geol.* **2016**, *423*, 7–18. [[CrossRef](#)]
31. Raymond, O.L. Pyrite composition and ore genesis in the Prince Lyell copper deposit, MtLyell mineral field, western Tasmania, Australia. *Ore Geol. Rev.* **1996**, *3*, 231–250. [[CrossRef](#)]
32. Chaussidon, M.; Lorand, J.P. Sulphur isotope composition of orogenic spinel lherzolite massifs from Ariege (North-Eastern Pyrenees, France): An ion microprobe study. *Geochim. Cosmochim. Acta* **1990**, *10*, 2835–2846. [[CrossRef](#)]
33. Li, J. *Typomorphic Characteristics and Genesis of Pyrite in the Gangcha-Kemo Area of Gansu Province*; Geological Publishing House: Beijing, China, 2016.

**Disclaimer/Publisher’s Note:** The statements, opinions and data contained in all publications are solely those of the individual author(s) and contributor(s) and not of MDPI and/or the editor(s). MDPI and/or the editor(s) disclaim responsibility for any injury to people or property resulting from any ideas, methods, instructions or products referred to in the content.